Investigation of photocatalytic and luminescence properties of Na0.5Ce0.5WO4 self-assembled photocatalysts under solar light irradiation: Morphological, temperature and pH role

Nadine Dirany, Virginie Chevallier, Oussam Hajjoul, Stéphane Mounier, Madjid Arab

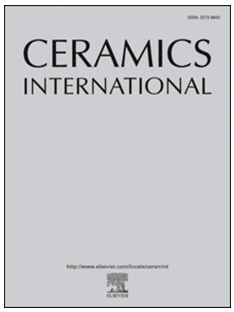

Investigation of photocatalytic and luminescence properties of $Na_{0.5}Ce_{0.5}WO_4$ self-assembled photocatalysts under solar light irradiation: Morphological, temperature and pH role

Nadine Dirany, Virginie Chevallier, Oussam Hajjoul, Stéphane Mounier, Madjid Arab

PII: S0272-8842(23)00205-5

DOI: https://doi.org/10.1016/j.ceramint.2023.01.185

Reference: CERI 35642

To appear in: *Ceramics International*

Received Date: 12 August 2022

Revised Date: 11 January 2023

Accepted Date: 27 January 2023

Please cite this article as: N. Dirany, V. Chevallier, O. Hajjoul, Sté. Mounier, M. Arab, Investigation of photocatalytic and luminescence properties of $Na_{0.5}Ce_{0.5}WO_4$ self-assembled photocatalysts under solar light irradiation: Morphological, temperature and pH role, *Ceramics International* (2023), doi: https://doi.org/10.1016/j.ceramint.2023.01.185.

Investigation of photocatalytic and luminescence properties of $Na_{0.5}Ce_{0.5}WO_4$ self-assembled photocatalysts under solar light irradiation: morphological, temperature and pH role

Nadine Dirany[1,2], Virginie Chevallier[1], Oussam Hajjoul[2], Stéphane Mounier[2], Madjid Arab[1*]

[1] Aix Marseille Université, Université of Toulon, CNRS, IM2NP, Marseille France, CS 60584, Toulon Cedex 9, F- 83041, France;

[2] Université de Toulon, Aix Marseille Université, CNRS/INSU, IRD, MIO UM 110, CS 60584-83041 Toulon CEDEX 9, France.

**Corresponding author email: madjid.arab@univ-tln.fr*

Abstract

Tungstate-based scheelite structures have attracted much attention for the photocatalytic,adsorption and luminescence. To improve their performance, several ways have been considered, such as morphology control, thermal treatment and nanostructuring materials. In this work, three uniform and homogeneous morphologies, such as spindles, spheres and flowers, of self-assembled three-dimensional $Na_{0.5}Ce_{0.5}WO_4$ were used as photocatalysts for methylene blue dye photodegradation under solar irradiation. Depending on morphology, they required different temperatures to reach crystallization. Thermal treatments at 500°C and 800°C resulted in changes in crystallite size, porosity, surface state, but also in bandgap and emission properties. Thus, the crystallite sizes are about 50 nm for samples (spindles and flowers) treated at 500°Cand 87-167 nm for those treated at 800°C. Their respective bandgap values measured by diffuse reflectance were 2.85 eV beyond 3.15 eV. The samples treated at 500°C showed a lower emission and a longer charge carrier lifetime. A strong trend to adsorption was revealed, especially at low pH value and for the samples treated at 500°C, reaching 100% at a pH value of 2.5. With decreasing pH, the photocatalysis activity increases (up to 50%), being also more efficient with catalysts treated at low temperature. It follows that the degradation efficiency of spindles treated at 500°C is clearly higher compared to other morphologies treated at different temperature, and suitable for solar photocatalysis.

Keywords: Tungstates, Nanostructure, photocatalyst, bandgap, fluorescence, lifetime.

Introduction

In recent years, considerable efforts in the field of materials science have been gradually devoted to the design and construction of three-dimensional (3D) self-assembled inorganic materials having homogeneous hierarchical structures. These efforts have been deployed not

only because of the fundamental scientific interest in studying the underlying mechanisms of self-assembly, but also because they allow the design of several functional materials with specific properties through precise control over the morphology, particles size and their self-assembly. From a technological point of view, applications as varied as photocatalysis, to remedy the major problems of environmental pollution, or the realization of optoelectronic devices may be targeted [1],[2].

In particular, tungstate (or molybdate) based materials of formula AWO_4 (or $AMoO_4$) (cations A = Ca, Sr, Cd, Ba), share the 3D hierarchical structure of scheelite. They are versatile materials that can be used as luminescent compounds and efficient phosphors, catalysts for wastewater treatment, ionic conductors [3],[4],[5],[6] [7],[8].

A large number of investigations have been performed to study and modify the luminescence and the photocatalytic properties of the AWO_4 based scheelite structures with and without doping. Among the routes studied, the partial substitution of A cations by rare earths allows the exploitation of new optoelectronic and chemical properties arising from the incompletely occupied 4f and the empty 5d electronic orbitals of the introduced rare earths. For example, L. He [9], and P. Jiang [10] reported that the cations can control the crystal structure, morphology and photoluminescence (PL) properties. A.K. Munirathnapp showed a pure phase of $Na_{0.5}Ce_{0.5}WO_4$ (NCWO) green phosphor as a potential candidate for solid state display and nonlinear optical applications [11],[12]**.** Durairajan et al. reported the color tunable Dy^{3+}/Tm^{3+} co-doped $NaGd(WO_4)_2$ phosphor for white light emission and for anisotropic transparent ceramic laser application [13]. X. Yu et al. showed the intense visible upconversion emission and near infrared luminescence of Er^{3+}/Yb^{3+} co-doped $NaGd(WO_4)$ nanoparticles [14]. Furthermore, M. C. Oliviera reported the role of the hexavalent cation (Mo^{6+} vs. W^{6+}) to design $BaW_{1-x}Mo_xO_4$ solid solution, such as substitution of W^{6+} by Mo^{6+} enhances the electron transfer process due to a stronger Mo(4d)-O(2p) hybridization than W(4d)-O(2p) [15].

These materials are also promising as photocatalysts and adsorbents. Indeed, the 3D hierarchical structure of scheelite, provided with porosity sites and different reactive faces, is favorable for adsorption/trapping of molecules and promote their diffusion. Tungstate (and molybdate) scheelite structures have been widely used as photocatalysts for organic pollutants degradation. C. Shivakumara reported the photocatalytic activity of AWO_4 scheelite structures for the degradation of methylene blue (MB) dye in acidic medium [16]. High photocalytic efficiency was verified for $BaPrWO_4$ crystals in the degradation of rhodamine B (RhB) dye after 30 min [17].

Exploring another strategy than doping or substitution, X. Liu developed a new graphene/$SrWO_4$ nanocomposite showing a total photodegradation activity of methyl orange (MO), compared to $SrWO_4$ [18]. Furthermore, similar structures have been studied for photocatalytical water splitting into H_2 and O_2 under UV light irradiation.

Due to their large bandgap (greater than 4 eV), the photocatalysis process occurs mainly under UV light exposure [15],[16],[19],[20],[21]. However, development of solar light photosensitive materials is one of the most emerging challenges to explore new photocatalysts for the degradation of the organic pollutants. In the general framework of developing high efficiency and low-cost wastewater remediation technologies, we report for the first time a study of trivalent cerium and sodium double tungstate $Na_{0.5}Ce_{0.5}WO_4$ as a photocatalyst under solar light illumination. We developed an EDTA-mediated hydrothermal synthesis route giving rise to various $Na_{0.5}Ce_{0.5}WO_4$ morphologies (spindles, spheres and flowers), such as structural and morphological parameters can be controlled [22]. To date, we focused our investigations on their photodegradation and photosensitive properties.

In this work, their photocatalytic performances were studied via the degradation of methylene blue (MB). All the materials obtained, thermally treated up to 800°C, were analyzed by X-Ray diffraction (XRD) and scanning electron microscopy (SEM), respectively for structural and morphological characterization. The photosensitive properties were investigated using first UV – Vis diffuse reflectance spectroscopy (DRS) based on the evaluation of the optical bandgap (Eg), and secondly fluorescence spectroscopy combined with the resolved decay time to emission spectra and the lifetime of the charge carriers.

Particular attention was paid to the effect of pH of the aqueous medium and the role of morphologies on the photo-degradation activity. This study addresses the correlation of the photocatalysis process with the morphological changes induced by the thermal treatment.

1. Experiment

1.1. Synthesis approach

All chemical products were obtained as follow: sodium tungstate hydrate powder from Alfa Aesar, cerium (III) nitrate hexahydrate and EDTA acid were purchased from Sigma Aldrich with high purification rate of 99 %. Sodium hydroxide and nitric acid are from Sigma Aldrich. All the syntheses and characterizations using water were carried out with 18 MΩ deionized water.

NCWO_spindles, spheres and flowers were synthesized through hydrothermal surfactant-assisted route. The synthesis of these crystals with different morphologies is detailed in our previous work [22]. In a typical procedure for preparing $Na_{0.5}Ce_{0.5}WO_4$ with different morphologies, Na_2WO_4,·$2H_2O$ powder and a fixed amount of EDTA (0.3 g) were separately dissolved in 14 ml of distilled water. Cerium nitrate hexahydrate (2 mmol) was added, then stirred for 20 min. After that, the precursor solution of Na_2WO_4,·$2H_2O$ was slowly added into the above solution, under continuous stirring. The pH of the mixed solution was maintained between 7 and 8 by adding dilute NaOH and HNO_3 solutions. The obtained yellow suspension was transferred into a 45 ml Teflon-lined stainless autoclave and heated at 200 °C for 24 h. Finally, the autoclave was cooled to room temperature and the precipitate was collected by centrifugation. The synthetic products were washed several times with distilled water and absolute ethanol. Then, the obtained powders were dried in an oven at 60 °C for 24 h. Finally, the collected powder was calcined at 500°C or 800 °C, according to the expected morphology, for 4 h in air, with a heating rate of 5 °C min^{-1}.

1.2. Characterization of the products

The NCWO crystals were structurally identified by XRD using an EMPYREAN Panalytical diffractometer, equipped with a copper X-ray source (wavelength λ=1.54 Å with a Ni filter eliminating the K_β radiation) with a step size of 0.0263º and a scan speed of 0.001 º/s. The diffraction analysis was carried out using *θ–2θ* configuration in the range of 10-80° and processed using the HighScore software package (PANalytical, 2003).

The crystallite sizes were evaluated from the corrected FWHM (full width at half maximum) of the diffraction peaks using the following Debye-Sherrer relation $D = \frac{K\lambda}{\Delta 2\theta \cos\theta}$, where D is the mean crystallite size, K is the form factor (K = 0.9 in the case of Gaussian profiles), λ is the radiation wavelength, β is the angular broadening of the Bragg peaks due to the size effect and θ is the Bragg angles in radians. The β value was calculated using a Gaussian approximation of peak profiles: $(\Delta 2\theta)^2 = (FWHM)^2 - \omega^2$, where ω is the FWHM corresponding to the standard NCWO sample.

The morphologies of different microcrystals were observed using a SUPRA 40Vp Colonne Gemini Zeiss scanning electron microscope (SEM) operated at 10 kV. The coupled energy dispersive spectroscopy analyzer (EDS) was used to analyze the local chemistry and the

microstructure of the NCWO crystals. All particle sizes were obtained using the Digital-micrograph software.

Photosensitive properties were investigated using first UV-Vis absorption spectra using a SHIMADZU 2600 UV-Vis spectrometer, in diffuse reflectance mode DRS with a 150 mm integrating sphere. The measurements were performed in the range of 250 to 800 nm at room temperature with a resolution of 0.08 nm and a reflectance accuracy of 0.005.

The optical bandgap energies Eg values were deduced from Kubelka – Munk relation, which is based on the transformation of the diffuse reflectance measurements. The Kubelka – Munk function $F(R_\infty)$ for any wavelength is described by :

$$F(R_\infty) = {K}/{S} = {(1 - R_\infty)^2}/{2R_\infty} \qquad \text{Eq. 1}$$

where R_∞ designates the absolute reflectance of the sample at infinite thickness [22]. K represents the molar absorption coefficient and S is the scattering coefficient. The optical bandgap can be deduced by the following equation:

$$(\alpha h\nu)^2 = A\left(h\nu - E_g\right)^n \qquad \text{Eq. 2}$$

where α is the absorption coefficient, hv corresponds to the incident photoenergy, A is a constant linked to the material. The index n corresponds to the electronic transition characteristic of the used semiconductor, that can be 1 for direct gap or 4 for indirect gap semiconductor. The scheelite structure $Na_{0.5}Ce_{0.5}WO_4$, is a direct bandgap semiconductor, so n = 1. Thus the bandgap energy of the obtained materials can be evaluated by extrapolating the linear part of the $(F(R) * h\nu)^2$ as a function of *hv* energy. In addition, the position of the conduction band (E_{CB}) and valence band (E_{VB}) of the catalysts have also been carried out by Mulliken electronegativity relations [23]:

$$E_{CB} = \chi - E_C - {1}/{2}\, E_g \qquad \text{Eq. 3}$$

$$E_{VB} = E_{CB} + E_g \qquad \text{Eq. 4}$$

where χ is the absolute electronegativity of the photocatalysts calculated by the geometric mean of the electronegativity of each element as : $\chi(A_aB_bC_cD_d) = \sqrt[a+b+c+d]{\chi(A)^a\chi(B)^b\chi(C)^c\chi(D)^d}$, E_C is the energy of the free electrons on the hydrogen scale (= 4.5 eV). According to the above

equations and the values of the bandgap and energy, band structures are displayed in table 1. Furthermore, the work function can be deduced from the following equation:

$$W = -E_{VB} + {}^{1}/_{2}\, E_g = -E_{CB} - {}^{1}/_{2}\, E_g \qquad \text{Eq. 5}$$

In the second time, the fluorescence spectra were carried out using the fluorescence spectroscopy photometer (FLUORIMAG, HORIBA) and the Time-Resolved Fluorescence (TRFL) were measured using a laser (284 nm) as excitation source.

The carriers' lifetimes is obtained from TRFL decay profiles of the samples combined with exponential decay fitting. The lifetimes are calculated according to the biexponential fitting equation: $I(t) = A_0 + A_1 \exp\left(\frac{t}{\tau_1}\right) + A_2 \exp\left(\frac{t}{\tau_2}\right)$ [24] and the average lifetime is deduced from $\tau_m = \frac{A_1\tau_1^2 + A_2\,\tau_2^2}{A_1 + A_2}$ [25], where A_0, A_1 *and* A_2 are weighting parameters of the decay component, τ_1 and τ_2 are carriers' lifetimes.

1.3. Photocatalytic experiment

The procedure consists of dispersing 100 mg of NCWO photocatalyst particles in 100 mL of an aqueous solution of MB dye, with a concentration of 1.15 10^{-5} M and a pH of 5.7 (called natural pH). The obtained suspension is stirred in the dark for 90 min, to achieve the adsorption - desorption equilibrium between the surface of the NCWO photocatalyst and the dyes molecules. The suspension was subsequently exposed to solar light irradiation provided by Philips lamps (tungsten lamp 300 W) fixed on a movable tray while stirring the suspension with a magnetic stirrer. At given periodic intervals of irradiation, 2 mL of the suspension were collected and centrifuged for 10 min at 10,000 rpm to remove catalyst powder and finally analyzed by a UV-Visible spectrometer, Shimadzu ™ UV-24646.

2. Results and discussion

2.1. Structural and morphological characterization

Phase identifications were performed from diffraction patterns using international ICSD data sheets. The identified phases were validated by Rietveld refinements, as reported in our previous work [22]. Fig. 1 shows the X-ray diffraction patterns of the three morphologies (spindle, flowers and sphere), as obtained from hydrothermal cell and then after heat treatment at 500 °C and 800 °C for 4 h. As can be seen from the diffractograms, the samples obtained after hydrothermal synthesis are not really crystallized with an identified phase, hence the need for heat treatments. As shown in Fig. 1, calcination at 500°C only allows crystallization of

spindles and flowers but not of spheres. The spindles and flowers are identified in scheelite like structure. The diffraction peaks can be assigned to the tetragonal phase of $CaWO_4$ of the space group $I4_1/a$ (n°88) in accordance with similar scheelite structures like $Na_{0.5}La_{0.5}WO_4$ and $Na_{0.5}Ce_{0.5}MoO_4$, respectively identified in ICSD database with 66090 and 67493 references. No additional peaks were detected, indicating the high purity of NCWO spindles and flowers. The higher thermal treatment, at 800°C, allows not only the crystallization of the spheres but also an improvement in the crystallization degree of the spindles and flowers samples, as evidenced by the presence of more intense and finer diffraction peaks.

Using Debye-Sherrer relation for each Bragg peaks of the X-ray pattern allowed us to estimate the crystallite size of each sample. The size values are around 50 nm for samples treated at 500°C and varie from 87 to 167 nm for samples treated at 800°C. This result is coherent with the expected growing of crystallites induced by heat treatment

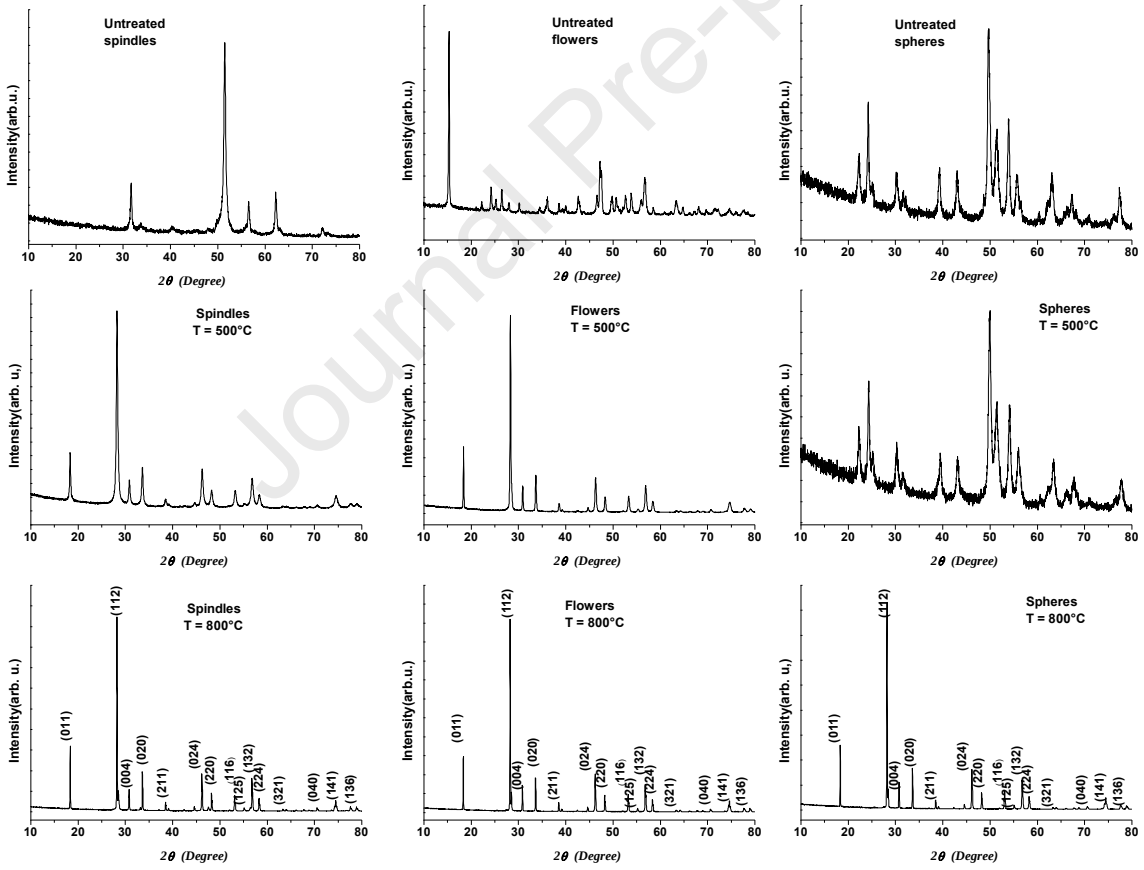

Fig. 1. X-ray diffraction patterns of NCWO obtained at different temperatures.

The refinement results confirm that the obtained materials are well crystallized in a scheelite-like structure with a space group of $I4_1/a$. The Na, Ce, W atoms' coordinates were identified in the Wyckoff positions. Nevertheless, we observed variations in the oxygen atomic coordinates,

giving rise to different polyhedral distortions [22]. It has been observed that the distance W – O increases as a function of the calcination temperature from 1.758 Å to 1.798 Å and the O – W – O angles are between 104° and 119°. At the same time, the M – O distance (where M indicates Ce or Na) decreases with the temperature, from 2.473 Å to 2.560 Å and the O – M – O angles varies between 73° and 136°. In addition to structuring, crystals show thermal and morphological stability.

Morphological investigation of the obtained samples were performed with SEM imaging. Fig. 2(a-f) show different forms of NCWO. The simultaneous control of the pH and EDTA concentration makes it possible to obtain various morphologies like spindles (SPL), spheres (SPR) and flowers (FLR). They vary from 0.30 to 0.35g and from 7 to 8, respectively for EDTA weight and pH, giving rise to homogeneous and regular samples. All of the structures obtained are self-assemblies of nanoparticles. The growth mechanism of different hierarchical structures is proposed and detailed in previous study [22]. Fig. 2(a) shows an example of the obtained spindles with a hierarchical construction from the 20 nm thick nanosheets. Reducing the pH to 7, while keeping the rest of the parameters unchanged, makes it possible to obtain spherical shaped structures rather than needles. This structure show uniform size and forms, with a mean diameter of the spheres around 8 μm. They were constructed from self-assembled 2D nanoplates with a thickness varying from 20 to 80 nm, and can be identified from surface roughness of the individual spheres, as observed in the SEM image (insert Fig. 2(c)). In the case of flowers, there self-assembly was obtained when the EDTA amount is increased to 0.35 g. Fig. 2(e) shows an homogeneous flowers sample, constructed from elongated flat and smooth nanoneedles. Individual nanoneedles exhibit mean thicknesse of about 300 nm. All morphologies present porosity between nanosheets/nanoplates/nanoneedles and surface cavities, leading to a differentiated surface area.

As mentioned previously, the calcination treatment allowed sample crystallization while modifying state surfaces. At 500°C, all morphologies remain intact, with the same surfaces characteristics, as observed in Fig. 2(a,c,e). However at 800°C, the surfaces states change with the loss of the hierarchical aspect following coalescence of elementary grains and inducing low porosity (see Fig. 2(b,d,f)). However, the general forms are kept with a slight decrease in size. The grains change with more facets and become rough for spindles while they became smooth respectively for spheres/flowers.

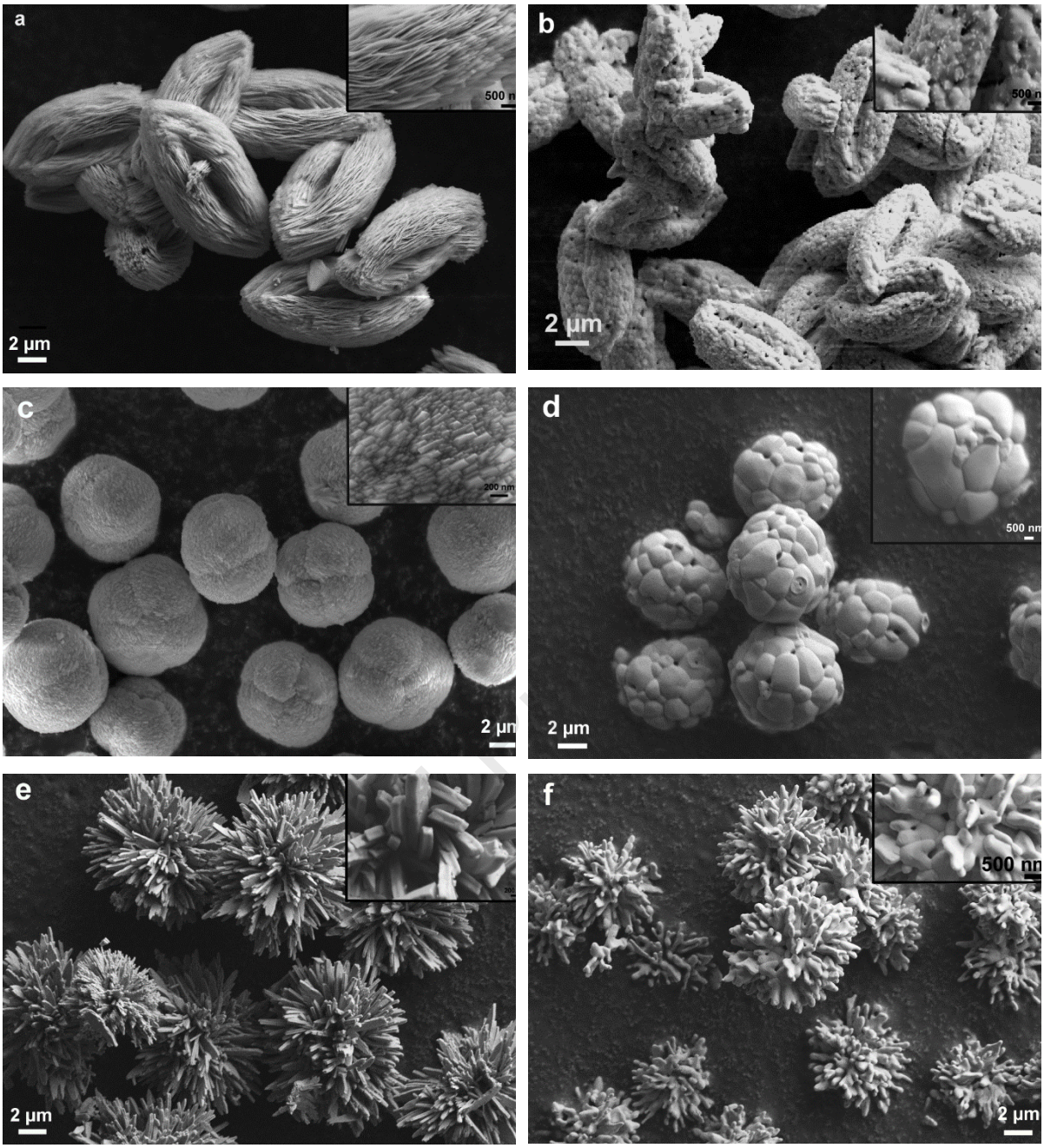

Fig. 2. SEM images of different NCWO samples morphologies: a, b) spindles, c,d) spheres and e,f) flowers treated at 500°C (a, c, e) and at 800°C (b, d, f). Insert pictures correspond to the magnification on elementary nanoparticles constituting the self-assembly.

2.2. Bandgap properties by diffuse reflectance spectroscopy

Semiconductor photocatalysts as photosensitive materials exhibit important structural, microstructural and morphological characteristics that are determinant in the representation of band structure. Then the gap is a parameter, which can determine the choice of the excitation wavelength range for photosensitive applications. Fig. 3 present the UV-Vis diffuse reflectance spectra of different morphologies. The absorption spectra shaw that the synthesized samples

exhibit sharp absorption peak from 375 nm, favoring use in the range of UV-Vis. This absorption occurs according to the electronic transition between valence and conduction bands. The associated band structure can be attributed to the transition from O 2p to Ce 4f+5d and W 4f states.

As shown in Fig. 3, globally the bandgap energy varies from 2.856 eV to 3.247 eV. The samples treated at 500°C present a lower energy than those treated at 800°C. In this case, we found that the bandgap energy value increases as a function of the nanoparticles' size. This behavior is in opposite trend of the classical semiconductors [26]-[27].

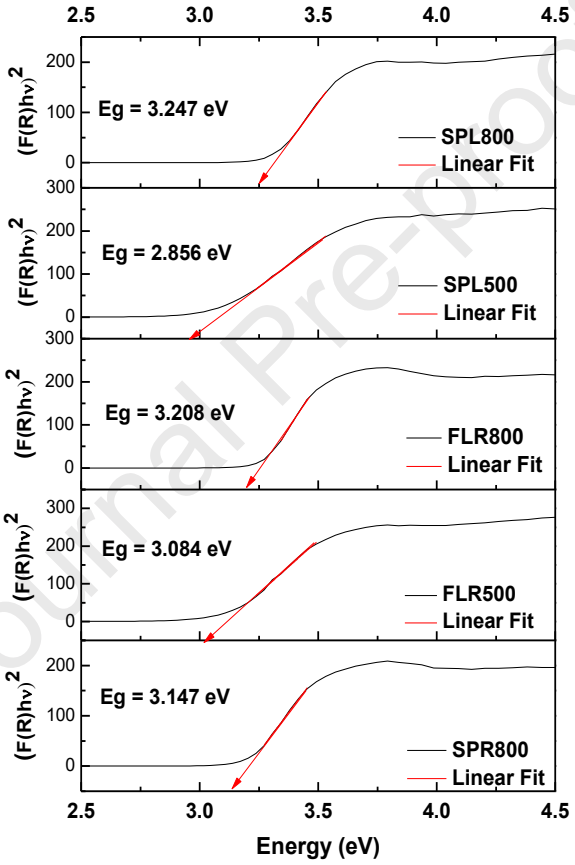

Fig. 3. Kubelka – Munk representation derived from the transformation of the diffuse reflectance measurements of NCWO photocatalysts.

Table 1
Energy levels of the associated band structure of the NCWO samples.

Samples	Temperature (°C)	Bandgap Eg (eV)	Conduction band E_{CB}	Valence band E_{VB}	Work W(eE)	Vaccum level (eV)
Spindles	500	2,85	-0,0071	2,8429	-1,4179	-5,9179
	800	3.24	-0,2021	3,0379	-1,4179	-5,9179

Flowers	500	3.08	-0,1221	2,9579	-1,4179	-5,9179
	800	3.20	-0,1821	3,0179	-1,4179	-5,9179
Spheres	800	3.14	-0,1521	2,9879	-1,4179	-5,9179

The obtained results show that the NCWO have a lower bandgap energy value than that which may be attributed to the microstructural order – disorder in the lattice [28]. The lowest values of the samples treated at 500°C suggest the existence of intermediate energy levels within forbidden bandgap, due to the low degree of crystallization, bonds distortions, vacancies and grains boundaries. The structural analysis conducted in previous work revealed high distortion of the WO_4 and AO_8 (A= Na, Ce) polyhedrals [22],[29]. The reported results show that strong distortions in O – W – O and O – A – O bonds cause a decrease of the bandgap.

Basically, the band structure of AWO_4 scheelite crystal depends only on O2p oxygen states for the valence band VB and W4f-5d tungsten states for the conduction band CB [30]. Furthermore, the Na orbitals do not appear in the forbidden band gap. Then, the lower bandgap of the obtained NCWO materials is due to the presence of Ce and to the structural distortions induced by heat treatment, depending on the morphologies and temperature. Apart from band structure studies on normal AWO_4 scheelite structures, to date no theoretical band structure studies have been reported in the literature on $Na_{0.5}Ce_{0.5}WO_4$. So for comparison, S. Ogo et al. reported theoretical investigation on deformed scheelite structure $Ce_{2/3}WO_4$ [31], which is close to the synthesized materials. They showed that Ce 4f orbital, localized below the fermi level, lies between the O2p bonding orbital and the W 5d antibonding orbital, indicating that the Ce 4f orbitals do not hybridize with W and/or O. In the scheelite structure, the Ce 4f orbital works as a donor orbital. These simulations show that the bandgap of the $Ce_{2/3}WO_4$ has a value of 2.89 eV, which are very close to the obtained band gap values of the samples processed at 500°C.

2.3. Fluorescence properties

The emission properties of the produced materials is related to the recombination of the charge carrier's possibilities. The luminescence spectra is usually used to investigate the separation and transfer efficiency of the photogenerated electron/holes during the photocatalytic process [32]. It is well known that the stronger luminescence indicates the faster recombination speed of the e/h charge carriers occurring during the oxidation and reduction reactions, resulting in lower photocatalytic efficiency.

Fig. 4 exhibits that the fluorescence profiles of samples reveal two broadband emission in the visible region with some defined peaks. The samples showed an intensive fluorescence peak in the blue region centered at 467 nm (2.65 eV) and a second strong emission in the red region at 536 nm (2.31 eV). The blue emission is related to the distorted WO_6 octahedra groups, while the red emission can be assigned both to the CeO_8 polyhedra and to CeO_x clusters, according to the rate of oxygen vacancies in the semiconductor. According to theoretical studies, *Ogo et al.* reported that the presence of Ce induced intermediate energy levels in the bandgap [31]. In addition to defects, the bandgap energy decreases and gives rise to the red emission, around 2.3 eV, as observed in our fluorescence spectra.

According to the spectra (fig. 4(a)), the emission intensities increase with temperature calcination and they are higher for samples with spindles and flowers morphologies than for spheres formed samples. We observed that the emission at 531 nm is lower for samples treated at 500°C than for those treated at 800°C, except for spindles, for which the emission band disappears at 800°C. It is no longer visible because the baseline is too high. However, the most intense peak at 560 nm is due to the second harmonic wavelength excitation.

Thus, it appears that increasing the crystallization degree enhances fluorescence, as the emission intensity increases with crystallite size. The increase in the heat treatment temperature leads to the decrease in the defect concentration and porosity with a larger sized crystallite. Samples treated at 500°C exhibiting almost the same crystallite size, show similar emissions spectra, without morphology effect. For samples calcined at 800°C, a morphological effect is observed, such as flowers shape samples fluoresce much stronger than spindles-shaped ones.

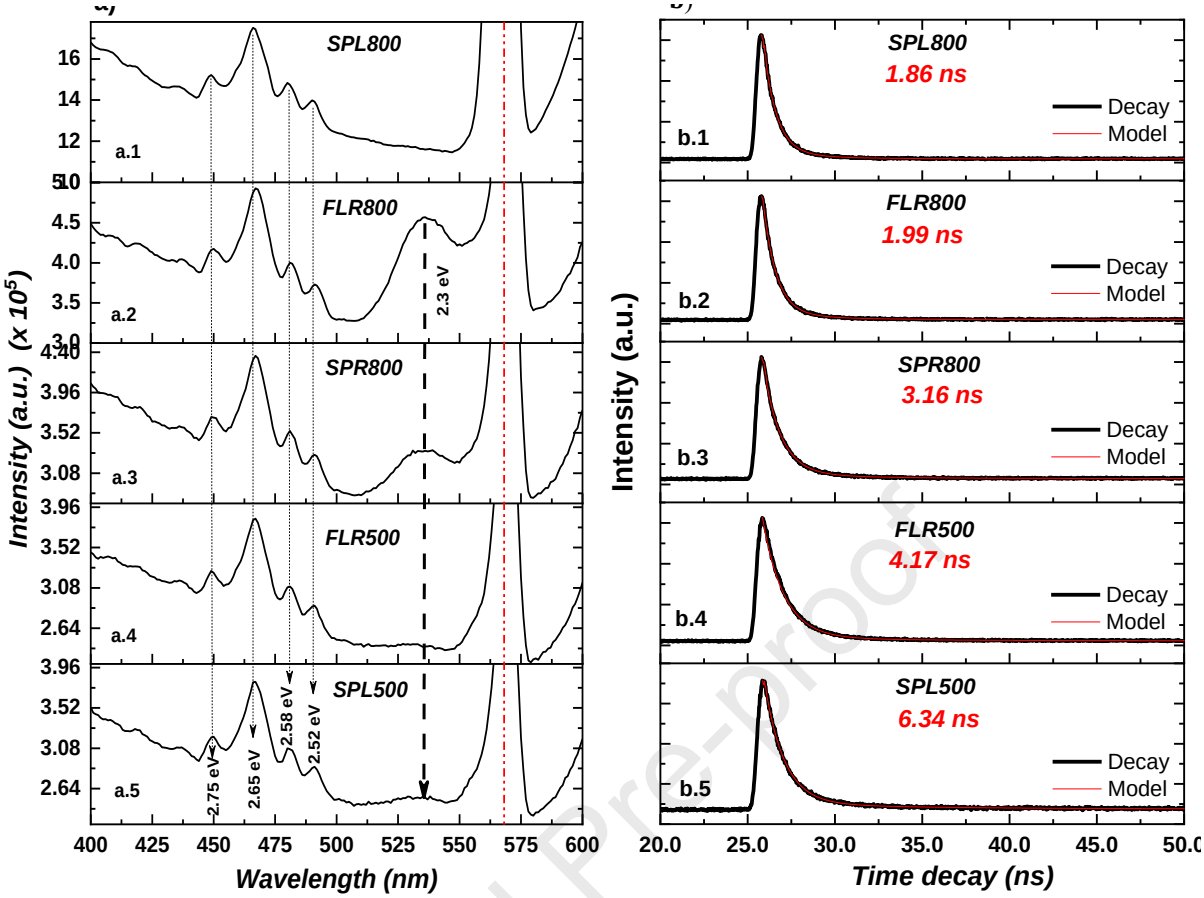

Fig. 4. a) Emission spectrum of the used samples and b) time resolved fluorescence spectra (TRFL) for the 468 nm emission.

As mentioned in the previous bandgap section, the presence of Ce induces the appearance of the Ce 4f levels, localized below the fermi level. The charge transfer is assigned to the W – O bonds within $(WO_4)^{2-}$ complex and to the 5d transition of Ce^{3+}. According to the literature data [22],[32], similar emissions were obtained in the case of the distorted scheelite structure $Ce_{2/3}WO_4$ with Tb doping. Without doping element, the broad emission may come from intrinsic electronic transitions of Ce^{3+}, either from Ce5d to Ce4f ground state, or from W5d to O2p/Ce4f. The broadband emission is due to the overlap of the energy levels Ce5d and Ce4f with W5d and O2p respectively.

Generally, the fluorescence is generated from the recombination of electron and holes charge carriers. As consequence, fluorescence spectra can be used as an indirect means of investigation of the separation and recombination capacity of charge carriers in the excited state of the materials. As shown in Fig. 4; the intensities depend particularly on the calcination temperature, as samples treated at 800°C fluoresce more intensively than those treated at 500°C. This suggests differentiated recombination lifetime of the photoinduced electron - holes charges

carriers. In this case, the time resolved fluorescence (TRFL) decay spectra is more suitable to investigate the charge carriers kinetics for quantifying the electron and holes separation efficiency.

The results of the fits show that the samples calcined at 800°C with stronger emission have a lower lifetime, than those treated at 500°C (Fig. 4(b)). The results are summarized in table 2.

Table 2
Lifetime values of the charge carriers recombination of different NCWO sample.

Samples	Lifetimes τ_m (ns)
Spindles 800C	1.86
Flowers 800C	1.99
Spheres 800C	3.16
Flowers 500C	4.17
Spindles 500C	6.34

2.4. Photocatalytic properties

Self-assembled materials with specific morphologies and varying porosity are excellent candidates for adsorption and photocatalysis applications. The $Na_{0.5}Ce_{0.5}WO_4$ hierarchical structures presented above are studied as catalysts or adsorbers (trapping) with the aim of eliminating organic waste which contaminates water. Among other dyes, methylene blue (MB) is often used as reference pollutant in photocatalytic studies. It is a cationic dye used in the textile industry, as a tracer element, but also in food. Its presence in industrial effluents generate a danger to aquatic and human lives. MB was used in this work to evaluate the photocatalytic activity of the elaborated structures.

a. MB dye degradation

The decomposition of the dye was carried out under solar light irradiation using a 300 W tungsten lamp. For all samples, wathever the morphology or heat treatment temperature, the pH of the obtained suspensions was 5.7 corresponding to the natural pH of MB solutions. They were maintained up to 90 minutes of stirring in the absence of light to reach the adsorption-desorption equilibrium. MB decomposition was followed by the intensity decrease and shift of the maximum absorption wavelength band (664 nm) observed on UV-Vis spectra recorded at different time intervals during irradiation. It appeared that the degradation process depends not only on the materials structuring/hierarchization but also on the basic or acid nature of medium.

As the active radicals evolved in the decomposition process change with the pH, it is crucial to prealably probe the role of pH to determine the range where the catalyst remains effective under irradiation. This study was realized with NCWO spindles-formed samples treated at 500°C (denoted SPL500 herafter) as photocatalyst, due to their better structural, morphological and optical properties, as discussed previously [22].

i. Role of the pH on the adsorption and photocatalytic efficiency

The pH effect on the degradation of MB dye in presence of SPL500 was analyzed in four media of different pH: 2.5, 3, 5.7 and 10. The pH adjustment to the desired values was carried out before irradiation, by adding a few drops of dilute solution of HCl or NaOH. Monitoring the concentration of pollutants during light irradiation was carried out by UV-visible absorption spectroscopy. The photocatalytic decomposition and/or the adsorption efficiency is defined from the following ratio: $\frac{C_0-C_n}{C_0}$, where C_0 and C_n respectively represent the initial concentration of MB (before adding the photocatalyst powder) and the concentration of MB at a given time (t=0 corresponding to the start of the irradiation so that negative times stand for the duration to reach sorption equilibrium).

As shown in Fig. 5(a), at natural pH (5.7), SPL500 enabled only a weak degradation of MB (24%) after 7 h of irradiation, while the photocatalysis of MB in the media of pH = 2.5, 3 and 10 respectively showed yields of the order of 100%, 85% and 50%.

Kinetics profiles revealed that the bleaching of the solution resulted from two distinct process : a first stage linked to the adsorption phenomenon and which occurs mainly in the dark, then, a second degradation due to the photoinduced activity under solar light irradiation. For this cationic dye, the adsorption setup is quite significant in acidic medium, with a very high yield and faster kinetics compared to other environments (See Fig. 5 (a-b)).

The adsorption process depends particularly on the pH of the medium: the fixation rate of MB molecules is negligible at pH 5 (around 2%), while a slight rise is registered in basic environment up to 17% at pH 10. However, the adsorption increases much more strongly in acidic conditions, reaching a rate of 47% at pH 3 and finally total adsorption for a pH of 2.5 or less. Furthermore, the catalysts turn blue after this adsorption step, such that the coloration is more and more marked with low pH. Thus, the photoinduced process alone achieved degradation rates of 20%, 32% and 40% of MB at pH of 5.7, 10 and 3 respectively.

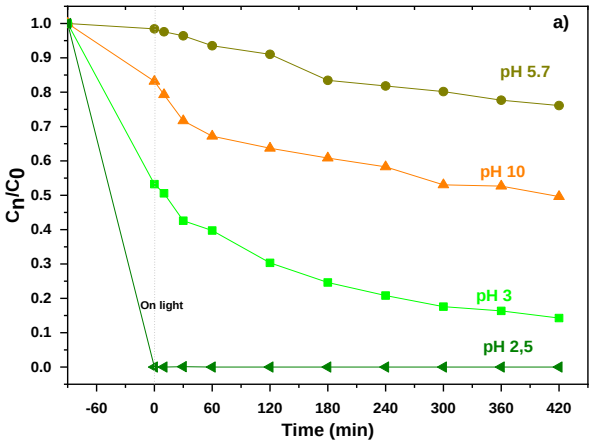

Fig. 5. Photocatalysis activity on SPL500C: Effect of pH on the adsorption and photocatalytic degradation performance of MB.

The results obtained show that the dye adsorption is a crucial and important step in the pollutant removal process at low pH (in acidic medium). Changing the pH of the suspension changes the charges, whether on the surface of the dye and/or on the oxide catalysts, inducing modifications of their interactions. Even if adsorption is not strictly speaking a degradation process, it is a valuable mean to consider in the purpose of water depollution control. Substances with high capacities to adsorb the dye offer rapid and significant dye removal solutions. But in the case of compounds developed for photocatalysis, strong adsorption properties can be either detrimental or beneficial. Indeed, several authors have shown that the influence of pH on the photocatalytic activity is related to the quantity of molecules adsorbed on the photocatalyst surface, as degradation occurs mainly there rather than in the solution [33],[34]. Promoting adsorption by increasing the interactions between the pollutant molecules and the surface is favourable if the degradation reaction occurs and desorption of the products ensues. But if the adsorption is too high and not reversible, it can prevent photons from reaching the surface and activating the catalyst, resulting in a decrease in photocatalytic activity.

NCWO adsorption ability may be associated to electrostatic attractions and/or hydrogen bonds between the dyes and the catalyst surface. On the one hand, the tungstate oxyanions WO_4^{2-}present on the surface give it a strong bronsted acid character. They can be hydroxylated or not depending on the pH of the solution, which modifies the surface charge of the catalyst. As already mentioned, MB is a cationic dye when dissolved in water, which will be noted MB^+ hereafter. At low pH, the catalyst surface is negatively charged and thus very attractive for cationic species such as MB^+. In addition, the non-bonding pairs of the terminal oxoligands can establish hydrogen bonds with the hydrogens of the amino groups of MB^+. Thus for pH 3, MB

interacts more actively on the surface of SPL500 with its two uncharged amino groups, than with the positively charged sulfonium group.

On the other hand, tungstate anions are Lewis bases of polyoxometalate nature; they exhibit relatively high adsorption activities with cationic dyes [35]. This adsorption activity becomes greater in an acidic medium at low pH (lower than 4). In this pH range (especially at pH 3), there is more active adsorption sites [26], which increases the number of molecules adsorbed and promotes better photocatalytic activity. Moreover, under acid conditions, the catalyst's charged surface can accelerate the transfer of electrons, which facilitates the separation of electron-hole pairs. Therefore, the number of oxidizing species responsible of the dyes photodegradation increases at low pH, accelerating the photocatalytic activity [36]. Electrons can react with O_2 adsorbed on the surface of the photocatalyst and with O_2 dissolved in solution to produce $O_2^{\bullet -}$ radicals. In addition, the h^+ holes become very active under acidic conditions and are responsible for the catalytic degradation of MB.

ii. Effect of the morphology on the degradation process

Photodegradation tests carried out at various pH value revealed a much better photocatalytic activity of SPL500, for pH 3, a pH value that minimized the adsorption part of the MB removal. Thus, this pH value was selected, to study the influence of the morphology and heat treatment temperature of the different NCWO microstructures on the adsorption and photocatalytic degradation of MB dye.

The monitoring of the MB photocatalytic degradation by various NCWO morphologies is shown in Fig. 6. The absorption intensities gradually decrease with time, well over 50%, in the presence of the different structures of NCWO. After 7 hours of irradiation, there is still a gradual decrease in the intensity of the MB band absorption. The color of the solution changes from dark blue to a very light blue indicating removal of the MB from the solution. The global removal efficiencies obtained by spindles (SPL500 and SPL800), flowers (FLR500 and FLR800) and spheres (SPR800), are respectively 86%, 65%, 71%, 50% and 54%.

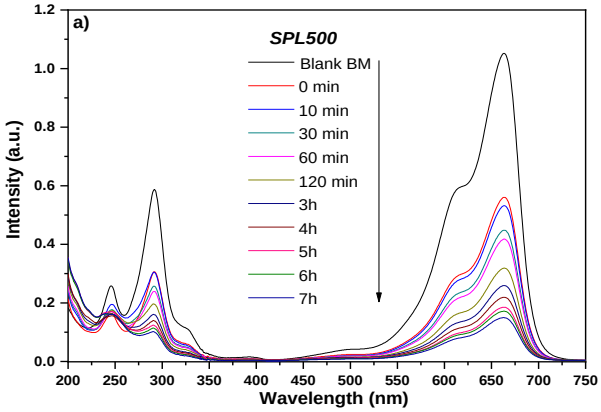

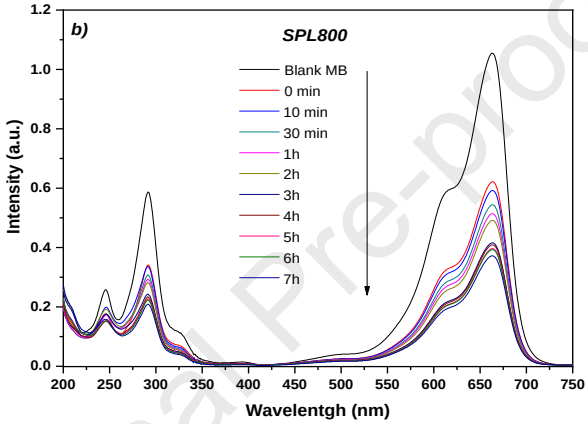

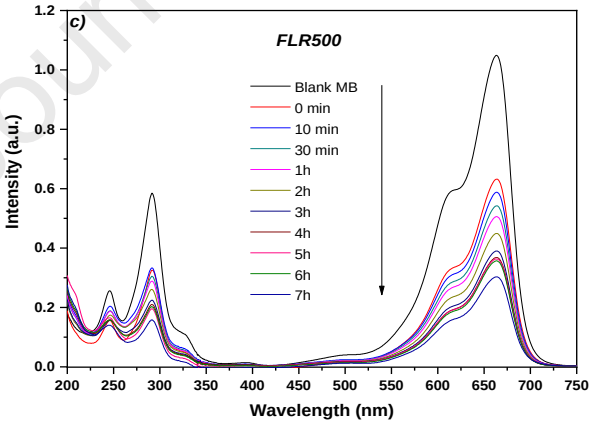

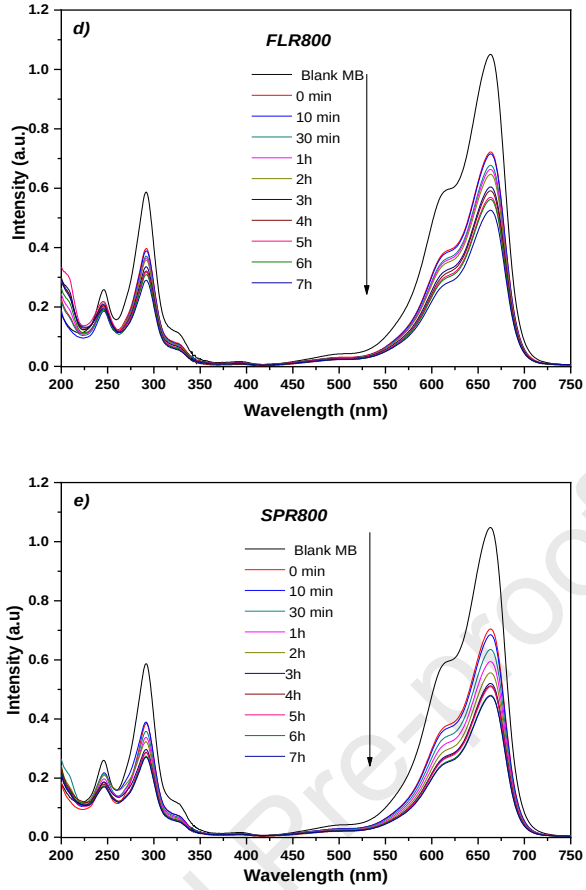

Fig. 6. UV-Vis spectra of MB degradation over different hierarchical NCWO structures **a)** SPL500 ; **b)** SPL800 ; **c)** FLR500C ; **d)** FLR800 and **e)** SPR800.

The detailed analysis of the MB removal process, revealed first a high adsorption rate in the dark, from 30% to 50% according to the sample, then followed by a photocatalysis process under irradiation, from 10% to 40%. All results of the adsorption and photoinduced rate degradation are summarized in the table 3. Globally, samples treated at 500°C showed both strong adsorption and a better photo-decomposition, almost twice as high as those treated at 800°C. The decrease in the adsorption rate is due to the thermal treatment, which induced a modification in the surface state. During the solar light irradiation, the MB photocatalysis activity revealed a decomposition rate of 40% and 31% respectively for SPL500 and FLR500. This activity becomes weaker, of the order of 24%, 18% and 21% respectively for SPL800, FLR800 and SPR800.

Globally, the crystallite size increases with calcination temperature such as the spindles and flowers respectively triple and double in size (167 nm and 113 nm), while the spheres size of SPR800 is around of 87 nm. Consequently, the surface area and the porosity decrease. As a result, there are fewer active sites compared to the sample treated at 500°C.

Similar work were conducted using a distorted scheelite $Ce_{2/3}MoO_4$ with different morphologies treated at 1000°C [37]. The MB photocatalytic tests were carried out during 96h under visible light irradiation. M. Dong reported a total degradation of 23%, 70%, 89% corresponding to the flowers, spheres and bundles, respectively. At the same irradiation time (for 7h), $Ce_{2/3}MoO_4$ showed a degradation of 45%, including both adsorption and photodecomposition. This rate remains equivalent to that obtained by FLR800 and almost twice as low as that of the SPL500. Lin X. et al. reported the application of 3D hierarchical $NaCeMoO_4$ structures as photocatalysts of cationic pollutant, Rhodamine B [38]. $Na_{0.5}Ce_{0.5}MoO_4$ microflowers with bimodal pores exhibited an adsorption performance for the removal of Rhodamine B (RhB) during 12h to reach a complete degradation. This absorption capability is attributed to the combination of the intrinsic property and morphological feature of the hierarchical microflowers.

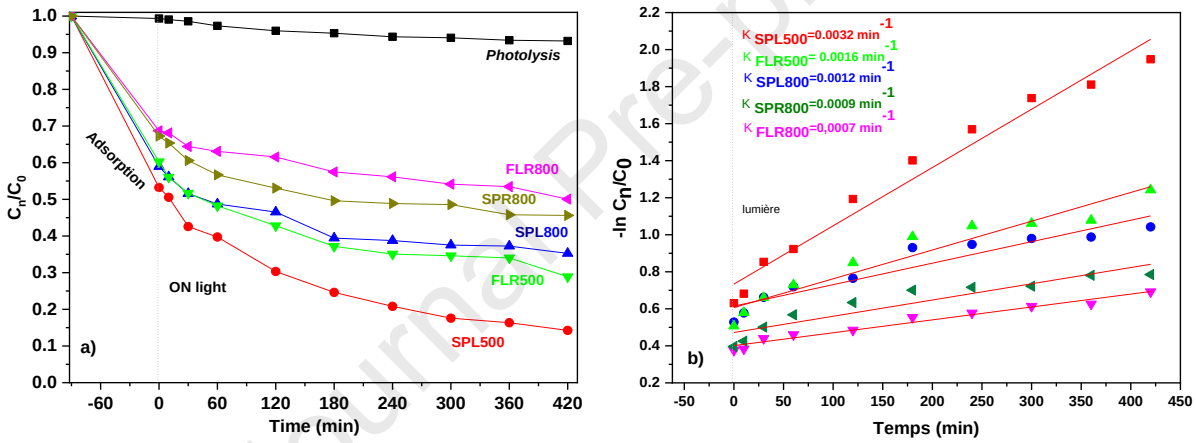

Fig. 7. a) MB degradation efficiency over different hierarchical structures; b) Photocatalytic degradation kinetics of different NCWO morphologies.

As shown in Fig. 7, all NCWO photocatalysts showed an efficiency for the MB degradation compared to the photolysis test performed. The kinetics of the degradation reaction are shown in Fig. 7(b). The adsorption and degradation rate follows a first order reaction, consistent with the general Langmuir-Hinshelwood mechanism [39] [40]:

$$-ln\frac{C_n}{C_0} = K_{app}t \qquad \text{Eq. 5}$$

where C_0 and C_n respectively represent the concentration of initial solution and the concentration of dyes at a given time t of irradiation.

From the plot of $ln\frac{C_n}{C_0}$ as a function of the irradiation time, we can estimate the first-order kinetic constant of the different morphologies. The kinetic constant K_{app} values of MB degradation and the crystallite sizes of the different NCWO photocatalysts used are shown in Table 3. From Fig. 5, 6 and the results of the table 1, it can be seen that the photocatalytic activity is highly dependent on morphology and calcination temperature. For a high adsorption rate of MB dye, the decomposition is also more important and faster. Globally, SPL500 and FLR500 exhibit the highest and the fastest photocatalytic activity compared to other NCWO morphologies treated at 800°C.

Table 3
Photo-catalytic efficiency and apparent kinetic constants of MB degradation by different NCWO structures.

NCWO Morphology	Temperature	Total Degradation rate (%)	Adsorption rate in the dark (%)	Degradation rate under light (%)	Apparent constant K_{app} (10^{-3} min^{-1})	R^2	Crystallite size (nm)	*Bandgap (eV)*
Spindles	500°C	86	47	41	3,2	0,979	51	*2,85*
	800°C	65	40	25	1,2	0,986	167	*3,24*
Flowers	500°C	71	40	31	1,6	0,969	52	*3,08*
	800°C	51	32	18	0,7	0,963	113	*3,20*
Spheres	800°C	54	33	21	0,9	0,958	87	*3,14*

b. General discussion

In this study, the evolution of the photocatalytic activity depends particularly on two factors, as summarized in table 3:

- The morphology and the surface states of the different self-assemblies.
- Heat treatment induced changes on the crystallites size and the bandgap energy.

The global degradation rates lies on two processes, firstly, the adsorption of molecules on the various surface active sites, and secondly, the photodecomposition under irradiation via redox processes. The degradation mechanism is based mainly on the nature and the number of adsorption sites that each structure can have via the catalyst hierarchization. Structuring by self-assembly gives rise to different surface states with a high microporosity that differs from one morphology to another. It generally constitutes active trapping sites for catalytic reactions [41], which enhances the photocatalytic activity. The structures, made up of an assembly of

elementary nanograins (nanoplatelets, nanodegs and nanosheets for flowers, spheres and spindles respectively), have large and deep cavities [22]. In addition to the classic surface reactivity, the porosity allows strong adsorption (trapping/confinement) and rapid diffusion of molecules.

In this configuration, the spindles obtained at 500°C exhibit better photocatalytic activity compared to that of spheres and flowers. This is due to the large number of nanosheets, and their low thickness (≤ 50 nm), while platelets and rods are about four times larger. This difference favors the appearance of narrow cavities but with a depth that can reach the width of the sheets. In the case of flowers, the self-assembly of the platelets resulted in large open spaces, favorable to adsorption, but with less confinement effect. This results in somewhat low adsorption and photodecomposition capacities compared to those of spindles. The spheres have a dense structure of platelets, but with very few porous surface. Nonetheless, this self-assembly generates very rough spheres, with numerous surface grooves as active sites, which appear between the pads.

The heat treatment at 800 °C led to a modification of the initial morphologies but also of the bricks size. The morphologies are maintained in their general form, of spindles, flowers and spheres. However, the calcination temperature rises at the loss of the hierarchical appearance of the structures as shown in Fig. 2. On the other hand, the surface states have evolved, and the coalescence phenomenon has given rise to submicron grains. The surface of these structures appears very smooth with lower porosity or even devoid of pores, which causes a decrease in their adsorption capacity and their photocatalytic reactivity.

The size of the elementary grains obtained after synthesis, as a function of the heat treatment, therefore has an influence on the catalytic properties and the surface reactions. This size generally conditions the specific surface area. In the case of spindles and flowers treated at 500°C, the crystallite size observed by SEM is of the order of 50 nm. However, the imagery reveals the existence of nanosheets constituting the spindles, much thinner than the platelets of the flowers. In the case of samples obtained at 800 °C, which exhibit a lower degradation rate, the crystallite size are larger: 167 nm for the spindles, 113 nm for the flowers and 87 nm for the spheres. However, we systematically observed a better decomposition rate for the spindles, compared to other morphologies at the same temperature. Finally, the degradation activity is better with samples obtained at low temperature, where the crystallite size is small. This trend is favored by lower bandgap of the structure treated at 500°C, rather close and sensitive to the visible light with wavelength above 400 nm. In addition, the fluorescence results showed a

higher luminescence intensity for samples treated at 800°C than those treated at 500°C. So, the previous structural and morphological observation are in agreement with fluorescence results, such as the intensities depend on the crystallization degrees rather on temperature treatment. As a consequence, the lifetime of the charge carriers is higher in the case of SPL500 and FLR500 compared to SPL800, FLR800 and SPR800 that corresponds respectively to 6.34, 4.17, 3.14, 1.99 and 1.86 ns. A slow emission rather favors longer lifetimes of charges carriers, such that the electrons-holes recombination is less rapid, favoring the active radical's formation involved in the photodegradation process.

Generally, porous structures reduce the reflection of light and promote its absorption. They also allow the binding and then transport of molecules to the active sites that are on the internal walls of structures [20]. These deep pores and large capacity allow hierarchical structures to be sufficiently impregnated with the dye solution promoting a high adsorption. Under irradiation, the structures absorb more photons to produce electron-hole pairs [41]. Thus, it appears that the small thickness (<50 nm) of the particles, such as that of the nanosheets, makes it possible to reduce the radiative recombination of the electron- hole pairs [20], which generates reactive species and allows a higher photocatalysis efficiency. This behavior is in agreement with our results, as in the case of spindles SPL500.

c. Photocatalysis mechanism of MB

During a photocatalytic process, two highly oxidizing radicals, $OH^{\bullet}$ and $O_2^{\bullet -}$ can be involved in the oxidative decomposition of polluting dyes. Their generation within the solution is the result of redox processes involving charge carriers photogenerated by irradiation of the photocatalyst: holes left in the BV (h_{BV}^{+}) and electrons transferred into the BC (e_{BC}^{-}) after absorption of radiations of energy greater than the band gap. However, the holes can only oxidize the water H_2O and hydroxyl ions adsorbed on the photocatalyst surface to produce the $OH^{\bullet}$ radical if their potential is more positive than the redox potential of the couple $H_2O / OH^{\bullet}$. Conversely, the BC electrons can only reduce the dissolved oxygen to form the $O_2^{\bullet -}$ radical if their potential is more negative than that of $O_2 / O_2^{\bullet -}$. The Fig. 10 clearly shows that none of the hierarchical NCWO structures in this study has the capacity to produce $O_2^{\bullet -}$ radicals, whereas they all have the ability to oxidize water or hydroxyl to produce $OH^{\bullet}$. Furthermore, it was reported that the presence of Ce^{3+} cations promoted the photodegradation by preventing the electrons/holes recombination [42], [43]. Therefore, only $OH^{\bullet}$ radicals are involved in the photodegradation process of MB. It is to be noticed that the redox potential of the couple

$H_2O/\ OH^\bullet$ decreases with increasing pH (on Fig. 10, the value is that obtained for a pH value of 0), so that the potential conditions remains favorable to produce $OH^\bullet$ radical even at high pH.

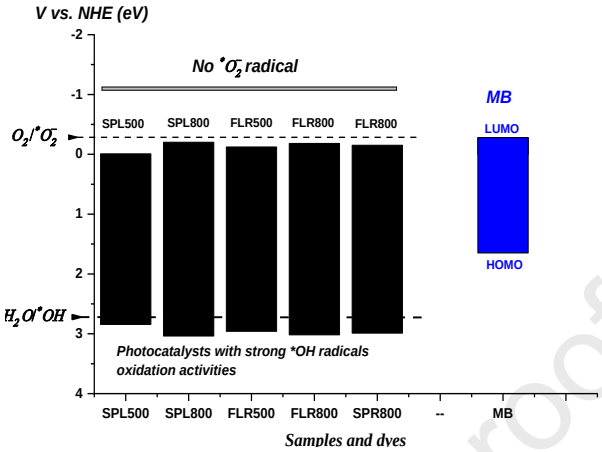

Fig. 10. schema of the samples and dyes band structures.

Generally, the photocatalysis of MB occurs according to two competitive processes: N-demethylation identified by shift towards shorter wavelengths of the main absorption band and destruction of the conjugated structure that is related to the decrease of the absorption bands located between 200 nm and 400 nm [44]. This study evidenced a heat-treatment temperature dependence of the MB degradation process : samples treated at 500°C allowed a destruction of the conjugated structures [45], as shown by the decrease of the peak at 250 nm, while with samples treated at 800°C, the UV-vis absorption spectra only revealed a decrease of the main band without any shift towards the short wavelengths.

The possible reactions which occur on the surface of the NCWO semiconductor and which lead to the degradation of the MB are as follows:

Table 4
Reactions of the MB decomposition over photocatalysts.

Light catalyst interaction and radicals generation	*Eq.*
$NCWO + h\nu \rightarrow NCWO\ (e_{BC}^- + h_{BV}^+)$	*6*
$NCWO\ (h_{BV}^+) + H_2O \rightarrow NCWO + H^+ + \ OH^\bullet$	*7*
$NCWO\ (h_{BV}^+) + OH^- \rightarrow NCWO + \ OH^\bullet$	*8*
$Dye_{ads} + \ h_{BV}^+ \rightarrow Oxydation\ products$	9
	10

$$Dye_{ads} + e_{BC}^{-} \rightarrow Reduction\ products$$

$$MB + OH^{\bullet} \rightarrow CO_2, NH_4^+, NO_3^-, SO_4^{2-}, Cl^- et\ H_2 \quad 11$$

As reported in section 2.1, the hierarchical spindles are formed by the self-assembly of a large number of superimposed nanosheets. This allows the generation of a large number of micropores or microcavities, resulting in a large specific surface area. This porosity promotes the diffusion of molecules, but also visible light, and therefore improves the photocatalysis efficiency [46]. The structuring of the spindles into finer nanosheets allows them to generate more $(h^+ - e^-)$ pairs, which favors the $OH^{\bullet}$ and $O_2^{\bullet -}$ radicals, and therefore, promotes the photocatalytic activity which becomes better than that of flowers and spheres.

Conclusions

In this work, we have reported the photosensitive, photocatalytic and adsorption properties of different scheelite structure $Na_{0.5}Ce_{0.5}WO_4$ based on three morphologies, spindles, spheres and flowers. Structural and morphological investigation revealed a single-phase crystallization of all obtained shape. Crystallization is achieved out from 500°C for spindles and flowers, and from 800°C for spheres. The crystallite size are about 50 nm for samples (spindles and flowers) treated at 500°C and 87-167 nm for those treated at 800°C. Thermal treatment showed the evolution of the morphology in size, porosity and surface state, suggesting short range in the order-disorder transition of the structures. The optical properties show a direct bandgap value lower than 2.85 eV for morphology treated at 500°C and beyond 3.15 eV for shapes treated at 800°C.

The degradation process involves two stages, firstly the adsorption of molecules on the various surface active sites, which is not properly speaking a degradation process, but contributes to remove the dye from water and secondly, the photocatalysis under visible light irradiation via redox reactions. Furthermore, the respective contributions of these two process to the total MB removal rate change with the pH of the reaction medium. We observed that both adsorption and photodegradation are more effective in an acidic environment than in a natural or basic environment, leading to much better total removal rate at acidic pH value. When the pH reach 2.5 or less, the process lies only on adsorption.

From a morphological point of view, the spindles seem to be more efficient than the others, with better adsorption and photocatalysis rates. As expected, the adsorption rate decreases with increasing heat treatment temperature, due to an increase in the crystallite size. In the case of

photocatalysis, the activity depends particularly on two factors, *i)* the morphology and the surface conditions of the different self-assemblies and *ii)* changes induced by heat treatment on the crystallites size and the bandgap.

Regarding these factors, spindles formed by self-assembly of nanosheets with a thickness of 20 nm and crystallite size of 50 nm, have a large specific surface area and a high porosity. As expected, this study revealed their largely superior performance compared to all other morphologies, both for MB adsorption and photodegradation. This spindles-shaped NCWO based photocatalyst is a promising candidate for organic waste depollution control.

Acknowledgment

We gratefully acknowledge the Regional Council of ProvenceAlpes-Côte d'Azur, General Council of Var, the Agglomeration Community of Toulon Provence Mediterranean and Toulon University for their support.

References

[1] H. Cölfen, M. Antonietti, Mesocrystals: Inorganic Superstructures Made by Highly Parallel Crystallization and Controlled Alignment, Angew. Chem. Int. Ed. 44 (2005) 5576–5591. https://doi.org/10.1002/anie.200500496.

[2] P. Jena, S.K. Gupta, N.K. Verma, A.K. Singh, R.M. Kadam, Energy transfer dynamics and time resolved photoluminescence in $BaWO_4:Eu^{3+}$ nanophosphors synthesized by mechanical activation, New J. Chem. 41 (2017) 8947–8958. https://doi.org/10.1039/C7NJ01249G.

[3] D. Das, S.K. Gupta, C.S. Datrik, P. Nandi, K. Sudarshan, Role of alkali charge compensation in the luminescence of $CaWO_4:Nd^{3+}$ and $SrWO_4:Nd^{3+}$ Scheelites, New J. Chem. 44 (2020) 7300–7309. https://doi.org/10.1039/D0NJ00651C.

[4] A. Azzouzi, M. Benchikhi, R. El Ouatib, Room-temperature co-precipitation synthesis of (Ca,Sr,Ba)WO4 solid solutions: Structural refinement, morphology and band gap tuning, Ceramics International. 46 (2020) 23706–23718. https://doi.org/10.1016/j.ceramint.2020.06.144.

[5] H. Wang, Y. Li, Z. Ning, L. Huang, C. Zhong, C. Wang, M. Liu, X. Lai, D. Gao, J. Bi, A novel red phosphor LixNa1-xEu(WO4)2 solid solution: Influences of Li/Na ratio on the microstructures and luminescence properties, Journal of Luminescence. 201 (2018) 364–371. https://doi.org/10.1016/j.jlumin.2018.05.015.

[6] X. Tan, Y. Wang, M. Zhang, Solvothermal synthesis, luminescence and energy transfer of Dy3+ and Sm3+ doped NaLa(WO4)2 nanocubes, Journal of Photochemistry and Photobiology A: Chemistry. 353 (2018) 65–70. https://doi.org/10.1016/j.jphotochem.2017.11.002.

[7] J. Wu, S. Du, Y. Wang, Photosensitizer coated upconversion nanoparticles for triggering reactive oxygen species under 980 nm near-infrared excitation, J. Mater. Chem. B. 7 (2019) 7306–7313. https://doi.org/10.1039/C9TB01629E.

[8] R.H. Damascena dos Passos, C. Pereira de Souza, C. Leroux, M. Arab, Catalytic properties of Sr1−xCexWO4: The role of mixed conduction in methane oxidation,

International Journal of Hydrogen Energy. 43 (2018) 15918–15930. https://doi.org/10.1016/j.ijhydene.2018.06.143.

[9] L. He, X. Zou, T. Wang, Q. Zheng, J. Liao, C. Xu, Y. Liu, D. Lin, Cation-Induced Variation of Micromorphology and Luminescence Properties of Tungstate Phosphors by a Hydrothermal Method, Inorg. Chem. 55 (2016) 12944–12952. https://doi.org/10.1021/acs.inorgchem.6b02352.

[10] P. Jiang, W. Gao, R. Cong, T. Yang, Structural investigation of the A-site vacancy in scheelites and the luminescence behavior of two continuous solid solutions $A_{1–1.5x}Eu_x□_{0.5x}WO_4$ and $A_{0.64–0.5y}Eu_{0.24}Li_y□_{0.12–0.5y}WO_4$ (A = Ca, Sr; □ = vacancy), Dalton Trans. 44 (2015) 6175–6183. https://doi.org/10.1039/C5DT00022J.

[11] L. Xu, J. Shen, C. Lu, Y. Chen, W. Hou, Self-Assembled Three-Dimensional Architectures of $Y_2(WO_4)_3$:Eu: Controlled Synthesis, Growth Mechanism, and Shape-Dependent Luminescence Properties, Crystal Growth & Design. 9 (2009) 3129–3136. https://doi.org/10.1021/cg801068k.

[12] L.S. Cavalcante, J.C. Sczancoski, L.F. Lima, J.W.M. Espinosa, P.S. Pizani, J.A. Varela, E. Longo, Synthesis, Characterization, Anisotropic Growth and Photoluminescence of $BaWO_4$, Crystal Growth & Design. 9 (2009) 1002–1012. https://doi.org/10.1021/cg800817x.

[13] A. Durairajan, D. Balaji, K.K. Rasu, S. Moorthy Babu, Y. Hayakawa, M.A. Valente, Sol–gel synthesis and photoluminescence studies on colour tuneable Dy3+/Tm3+ co-doped NaGd(WO4)2 phosphor for white light emission, Journal of Luminescence. 157 (2015) 357–364. https://doi.org/10.1016/j.jlumin.2014.09.024.

[14] X. Yu, M. Gao, J. Li, L. Duan, N. Cao, Z. Jiang, A. Hao, P. Zhao, J. Fan, Near infrared to visible upconversion emission in Er3+/Yb3+ co-doped NaGd(WO4)2 nanoparticles obtained by hydrothermal method, Journal of Luminescence. 154 (2014) 111–115. https://doi.org/10.1016/j.jlumin.2014.04.016.

[15] M.C. Oliveira, J. Andrés, L. Gracia, M.S.M.P. de Oliveira, J.M.R. Mercury, E. Longo, I.C. Nogueira, Geometry, electronic structure, morphology, and photoluminescence emissions of BaW1-xMoxO4 (x = 0, 0.25, 0.50, 0.75, and 1) solid solutions: Theory and experiment in concert, Applied Surface Science. 463 (2019) 907–917. https://doi.org/10.1016/j.apsusc.2018.08.146.

[16] C. Shivakumara, R. Saraf, S. Behera, N. Dhananjaya, H. Nagabhushana, Scheelite-type MWO4 (M=Ca, Sr, and Ba) nanophosphors: Facile synthesis, structural characterization, photoluminescence, and photocatalytic properties, Materials Research Bulletin. 61 (2015) 422–432. https://doi.org/10.1016/j.materresbull.2014.09.096.

[17] L.S. Cavalcante, F.M.C. Batista, M.A.P. Almeida, A.C. Rabelo, I.C. Nogueira, N.C. Batista, J.A. Varela, M.R.M.C. Santos, E. Longo, M. Siu Li, Structural refinement, growth process, photoluminescence and photocatalytic properties of (Ba1-xPr2x/3)WO4 crystals synthesized by the coprecipitation method, RSC Adv. 2 (2012) 6438. https://doi.org/10.1039/c2ra20266b.

[18] X. Liu, Y. Nie, H. Yang, S. Sun, Y. Chen, T. Yang, S. Lin, Enhancement of the photocatalytic activity and electrochemical property of graphene-SrWO 4 nanocomposite, Solid State Sciences. 55 (2016) 130–137. https://doi.org/10.1016/j.solidstatesciences.2016.03.006.

[19] N. Dirany, A. Hallaoui, J.C. Valmalette, M. Arab, Effect of morphology and temperature treatment control on the photocatalytic and photoluminescence properties of $SrWO_4$ crystals, Photochem. Photobiol. Sci. 19 (2020) 235–250. https://doi.org/10.1039/C9PP00331B.

[20] V.M. Longo, L.S. Cavalcante, E.C. Paris, J.C. Sczancoski, P.S. Pizani, M.S. Li, J. Andrés, E. Longo, J.A. Varela, Hierarchical Assembly of $CaMoO_4$ Nano-Octahedrons

and Their Photoluminescence Properties, J. Phys. Chem. C. 115 (2011) 5207–5219. https://doi.org/10.1021/jp1082328.
[21] Y. Zheng, J. Lin, Q. Wang, Emissions and photocatalytic selectivity of SrWO4:Ln3+ (Eu3+, Tb3+, Sm3+ and Dy3+) prepared by a supersonic microwave co-assistance method, Photochem. Photobiol. Sci. 11 (2012) 1567. https://doi.org/10.1039/c2pp25184a.
[22] N. Dirany, M. Arab, A. Moreau, J.Ch. Valmalette, J.R. Gavarri, Hierarchical design and control of NaCe(WO $_4$) $_2$ crystals: structural and optical properties, CrystEngComm. 18 (2016) 6579–6593. https://doi.org/10.1039/C6CE01340F.
[23] A. Esfandiar, A. Irajizad, O. Akhavan, S. Ghasemi, M.R. Gholami, Pd–WO3/reduced graphene oxide hierarchical nanostructures as efficient hydrogen gas sensors, International Journal of Hydrogen Energy. 39 (2014) 8169–8179. https://doi.org/10.1016/j.ijhydene.2014.03.117.
[24] A. Verma, D.P. Jaihindh, Y.-P. Fu, Photocatalytic 4-nitrophenol degradation and oxygen evolution reaction in CuO/g-C $_3$ N $_4$ composites prepared by deep eutectic solvent-assisted chlorine doping, Dalton Trans. 48 (2019) 8594–8610. https://doi.org/10.1039/C9DT01046G.
[25] X. Zheng, Z. Wang, T. Chen, J. Ran, Y. Wu, C. Tan, Q. Zhang, P. Chen, F. Wang, H. Liu, W. Lv, G. Liu, One-step synthesis of carbon nitride nanobelts for the enhanced photocatalytic degradation of organic pollutants through peroxydisulfate activation, Environ. Sci.: Nano. 8 (2021) 245–257. https://doi.org/10.1039/D0EN00985G.
[26] R. Lacomba-Perales, J. Ruiz-Fuertes, D. Errandonea, D. Martínez-García, A. Segura, Optical absorption of divalent metal tungstates: Correlation between the band-gap energy and the cation ionic radius, Europhys. Lett. 83 (2008) 37002. https://doi.org/10.1209/0295-5075/83/37002.
[27] A.P. Alivisatos, Semiconductor Clusters, Nanocrystals, and Quantum Dots, Science. 271 (1996) 933–937. https://doi.org/10.1126/science.271.5251.933.
[28] V.M. Longo, E. Orhan, L.S. Cavalcante, S.L. Porto, J.W.M. Espinosa, J.A. Varela, E. Longo, Understanding the origin of photoluminescence in disordered Ca0.60Sr0.40WO4: An experimental and first-principles study, Chemical Physics. 334 (2007) 180–188. https://doi.org/10.1016/j.chemphys.2007.02.025.
[29] N. Dirany, M. Arab, V. Madigou, Ch. Leroux, J.R. Gavarri, A facile one step route to synthesize WO $_3$ nanoplatelets for CO oxidation and photodegradation of RhB: microstructural, optical and electrical studies, RSC Adv. 6 (2016) 69615–69626. https://doi.org/10.1039/C6RA13500E.
[30] M. Song, Q. Zhang, T. Liu, J. Yin, X. Guo, H. Zhang, X. Wang, First-principles study on electronic states of SrWO4 crystals containing F-type color centers, Current Applied Physics. 9 (2009) 812–815. https://doi.org/10.1016/j.cap.2008.07.014.
[31] S. Ogo, H. Nakatsubo, K. Iwasaki, A. Sato, K. Murakami, T. Yabe, A. Ishikawa, H. Nakai, Y. Sekine, Electron-Hopping Brings Lattice Strain and High Catalytic Activity in the Low-Temperature Oxidative Coupling of Methane in an Electric Field, J. Phys. Chem. C. 122 (2018) 2089–2096. https://doi.org/10.1021/acs.jpcc.7b08994.
[32] D. Das, S.K. Gupta, A.P. Srivastava, P. Utpalla, K. Sudarshan, Probing emission and defects in BaW $_x$ Mo $_{1–x}$ O $_4$ solid solutions: achieving color tunable luminescence by W/Mo ratio and size manipulation, New J. Chem. 44 (2020) 10380–10389. https://doi.org/10.1039/D0NJ01824D.
[33] P.V. Klevtsov, R.F. Klevtsova, Polymorphism of the double molybdates and tungstates of mono- and trivalent metals with the composition M+R3+(EO4)2, J Struct Chem. 18 (1977) 339–355. https://doi.org/10.1007/BF00753083.

[34] R.M. Hazen, L.W. Finger, J.W.E. Mariathasan, High-pressure crystal chemistry of scheelite-type tungstates and molybdates, Journal of Physics and Chemistry of Solids. 46 (1985) 253–263. https://doi.org/10.1016/0022-3697(85)90039-3.
[35] D. Errandonea, Landau theory applied to phase transitions in calcium orthotungstate and isostructural compounds, Europhys. Lett. 77 (2007) 56001. https://doi.org/10.1209/0295-5075/77/56001.
[36] P. Niu, Photocatalytic Degradation of Methyl Orange in Aqueous TiO2 Suspensions, Asian J. Chem. 25 (2013) 1103–1106. https://doi.org/10.14233/ajchem.2013.13539.
[37] M. Dong, Q. Lin, H. Sun, D. Chen, T. Zhang, Q. Wu, S. Li, Synthesis of Cerium Molybdate Hierarchical Architectures and Their Novel Photocatalytic and Adsorption Performances, Crystal Growth & Design. 11 (2011) 5002–5009. https://doi.org/10.1021/cg200904t.
[38] L. Xu, X. Yang, Z. Zhai, D. Gu, H. Pang, W. Hou, Self-assembled 3D architectures of NaCe(MoO4)2 and their application as absorbents, CrystEngComm. 14 (2012) 7330. https://doi.org/10.1039/c2ce25897h.
[39] J. Bandiera, C. Naccache, Kinetics of methanol dehydration on dealuminated H-mordenite: Model with acid and basic active centres, Applied Catalysis. 69 (1991) 139–148. https://doi.org/10.1016/S0166-9834(00)83297-2.
[40] M. Ammann, U. Pöschl, Y. Rudich, Effects of reversible adsorption and Langmuir–Hinshelwood surface reactions on gas uptake by atmospheric particles, Phys. Chem. Chem. Phys. 5 (2003) 351–356. https://doi.org/10.1039/B208708A.
[41] H. Yamagami, A. Hasegawa, Electronic Structure and Fermi Surface of $LaRu_2Si_2$, J. Phys. Soc. Jpn. 61 (1992) 2388–2398. https://doi.org/10.1143/JPSJ.61.2388.
[42] L. J. Burcham, I. E. Wachs, Vibrational analysis of the two non-equivalent, tetrahedral tungstate (WO4) units in Ce2(WO4)3 and La2(WO4)3, Spectrochimica Acta Part A: Molecular and Biomolecular Spectroscopy. 54 (1998) 1355–1368. https://doi.org/10.1016/S1386-1425(98)00036-5.
[43] W.-L. Feng, C.-Y. Tao, K. Wang, Synthesis and Photoluminescence of Tetravalent Cerium-Doped Alkaline-Earth-Metal Tungstate Phosphors by a Co-precipitation Method, Spectroscopy Letters. 48 (2015) 381–385. https://doi.org/10.1080/00387010.2014.890941.
[44] D. Christofilos, S. Ves, G.A. Kourouklis, Pressure Induced Phase Transitions in Alkaline Earth Tungstates, phys. stat. sol. (b). 198 (1996) 539–544. https://doi.org/10.1002/pssb.2221980172.
[45] A. Jayaraman, B. Batlogg, L.G. VanUitert, High-pressure Raman study of alkaline-earth tungstates and a new pressure-induced phase transition in BaW O 4, Phys. Rev. B. 28 (1983) 4774–4777. https://doi.org/10.1103/PhysRevB.28.4774.
[46] L.L.Y. Chang, M.G. Scroger, B. Phillips, Alkaline-Earth Tungstates: Equilibrium and Stability in the M-W-O Systems, J American Ceramic Society. 49 (1966) 385–390. https://doi.org/10.1111/j.1151-2916.1966.tb13291.x.

Declaration of interests

☒ The authors declare that they have no known competing financial interests or personal relationships that could have appeared to influence the work reported in this paper.

☐The authors declare the following financial interests/personal relationships which may be considered as potential competing interests:

Dr. Madjid ARAB